

WMamba: Wavelet-based Mamba for Face Forgery Detection

Siran Peng pengsiran2023@ia.ac.cn MAIS, CASIA; SAI, UCAS Beijing, China	Tianshuo Zhang tianshuo.zhang@nlpr.ia.ac.cn SAI, UCAS; MAIS, CASIA Beijing, China	Li Gao gaolids@chinamobile.com CMFT Co., Ltd. Beijing, China	Xiangyu Zhu xiangyu.zhu@ia.ac.cn MAIS, CASIA; SAI, UCAS Beijing, China
Haoyuan Zhang zhanghaoyuan2023@ia.ac.cn SAI, UCAS; MAIS, CASIA Beijing, China	Kai Pang pangkai@pixelall.com Guangzhou Pixel Solutions Co., Ltd. Guangzhou, China	Zhen Lei [*] zhen.lei@ia.ac.cn MAIS, CASIA; SAI, UCAS Beijing, China	CAIR, HKSIS, CAS Hong Kong, China SCSE, FIE, M.U.S.T Macau, China

Abstract

The rapid evolution of deepfake generation technologies necessitates the development of robust face forgery detection algorithms. Recent studies have demonstrated that wavelet analysis can enhance the generalization abilities of forgery detectors. Wavelets effectively capture key facial contours, often slender, fine-grained, and globally distributed, that may conceal subtle forgery artifacts imperceptible in the spatial domain. However, current wavelet-based approaches fail to fully exploit the distinctive properties of wavelet data, resulting in sub-optimal feature extraction and limited performance gains. To address this challenge, we introduce WMamba, a novel wavelet-based feature extractor built upon the Mamba architecture. WMamba maximizes the utility of wavelet information through two key innovations. First, we propose Dynamic Contour Convolution (DCConv), which employs specially crafted deformable kernels to adaptively model slender facial contours. Second, by leveraging the Mamba architecture, our method captures long-range spatial relationships with linear complexity. This efficiency allows for the extraction of fine-grained, globally distributed forgery artifacts from small image patches. Extensive experiments show that WMamba achieves state-of-the-art (SOTA) performance, highlighting its effectiveness in face forgery detection.

CCS Concepts

- Computing methodologies → Biometrics.

Keywords

Face Forgery Detection, Wavelet, Mamba

ACM Reference Format:

Siran Peng, Tianshuo Zhang, Li Gao, Xiangyu Zhu, Haoyuan Zhang, Kai Pang, and Zhen Lei. 2025. WMamba: Wavelet-based Mamba for Face Forgery

^{*}Corresponding author.



This work is licensed under a Creative Commons Attribution 4.0 International License.
MM '25, Dublin, Ireland

© 2025 Copyright held by the owner/author(s).

ACM ISBN 979-8-4007-2035-2/2025/10

<https://doi.org/10.1145/3746027.3755592>

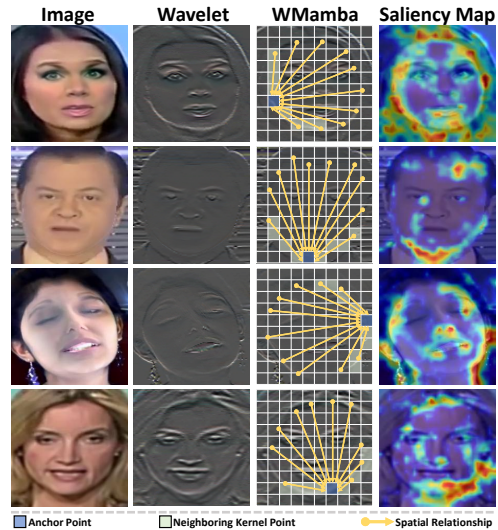


Figure 1: **Column 1:** Example frames from the FaceForensics++ (FF++) dataset [50]. **Column 2:** Wavelets capture facial contours that are often slender, fine-grained, and globally distributed. **Column 3:** WMamba maximizes the potential of wavelet data via two innovations: DCConv for precise modeling of slender facial contours (green squares) and Mamba [13] for extracting fine-grained and globally distributed forgery artifacts (yellow arrows). **Column 4:** Saliency maps generated by Grad-CAM [51] reveal that our model focuses on key facial contours, which are rich in forgery artifacts.

Detection. In *Proceedings of the 33rd ACM International Conference on Multimedia (MM '25)*, October 27–31, 2025, Dublin, Ireland. ACM, New York, NY, USA, 13 pages. <https://doi.org/10.1145/3746027.3755592>

1 Introduction

Recent advancements in deepfake generation technologies [22, 27, 31, 43, 53] have garnered significant attention due to their ability to produce highly realistic digital faces. While these technologies offer entertainment value, their potential for misuse, such as facilitating

fraud, spreading misinformation, and fabricating fake news, poses serious social risks. As a result, there is an urgent need for the development of robust face forgery detection algorithms.

Detecting facial forgery artifacts directly in the spatial domain presents inherent challenges due to their subtle and often imperceptible nature. Consequently, many approaches turn to frequency analysis techniques to reveal hidden manipulation traces [29, 48, 58]. Among these techniques, wavelet analysis has gained significant attention for its ability to capture intricate frequency components while preserving essential spatial characteristics [25, 30, 34, 40]. Specifically, wavelets effectively capture key facial contours that are **slender** (elongated and narrow), **fine-grained** (typically one to two pixels wide), and **globally distributed** (covering large regions across the entire image), as illustrated in Figure 1. These contours often encode subtle but informative forgery clues, making them crucial for manipulation detection, as shown in Figure 4. However, existing wavelet-based approaches rely on standard convolutions or Transformers [10] for feature extraction, which limits their ability to fully exploit the unique properties of wavelet information.

To tackle this challenge, we introduce WMamba, a wavelet-based feature extractor built upon the Mamba architecture [13]. WMamba fully considers the slender, fine-grained, and globally distributed nature of facial contours, maximizing the potential of wavelet information through two critical innovations. First, inspired by previous studies on deformable convolution [5, 44, 47, 62, 77], we present Dynamic Contour Convolution (DCCConv), which utilizes meticulously crafted deformable kernels to adaptively capture the **slender** structures of facial contours. Second, our method leverages the Mamba architecture, a highly effective alternative to traditional Convolutional Neural Networks (CNNs) and Transformers. Rooted in the State Space Model (SSM), Mamba excels at capturing long-range relationships while maintaining linear computational complexity. This efficiency facilitates the use of smaller image patches, enabling the extraction of **fine-grained** and **globally distributed** forgery artifacts. In conclusion, our main contributions are as follows:

- We propose Dynamic Contour Convolution (DCCConv), an innovative variant of deformable convolution that employs carefully designed deformable kernels to adaptively and precisely capture the slender structures of facial contours.
- We demonstrate the effectiveness of the Mamba architecture in detecting facial forgeries. Mamba excels at capturing long-range dependencies while maintaining linear computational complexity, which allows it to extract fine-grained, globally distributed facial forgery clues from small image patches.
- By combining DCCConv with Mamba, the proposed WMamba fully leverages the potential of wavelet information. Extensive experimental results show that WMamba achieves state-of-the-art (SOTA) performance, underscoring its exceptional capabilities in the field of face forgery detection.

2 Related Works & Motivation

2.1 Face Forgery Detection

According to [45], existing studies on face forgery detection can be broadly categorized into four types based on the strategies they employ: spatial-domain, frequency-domain, time-domain, and data-driven approaches. Spatial-domain methods detect facial forgeries

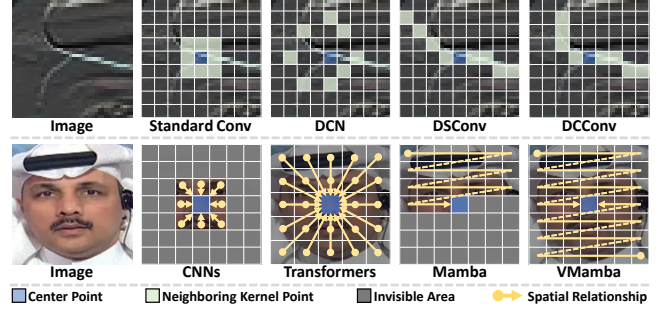


Figure 2: **Row 1:** Graphical comparison of different convolutional paradigms for capturing slender structures. Standard convolutions and DCN struggle with such structures, DSConv offers limited representation, while DCCConv demonstrates superior capability. **Row 2:** Graphical comparison of global perception capabilities. Only two flattening directions of VMamba are visualized. CNNs lack global perception ability. Transformers capture global context but require splitting the input image into larger patches due to quadratic complexity. Mamba exhibits partial global perception, while VMamba demonstrates enhanced global perception capability.

by examining variations in spatial details at the image level, such as color [21], saturation [39], and artifacts [3, 4, 52, 68, 71]. In contrast, time-domain methods analyze inter-frame inconsistencies, leveraging the entire video as input to identify manipulations [14–16, 19, 46, 67, 70]. Frequency-domain methods employ algorithms such as the Fast Fourier Transform (FFT) [58], Discrete Cosine Transform (DCT) [29, 48], and Discrete Wavelet Transform (DWT) [25, 30, 34, 40] to convert data from the spatial or time domain into the frequency domain. These techniques are particularly effective in uncovering subtle forgery traces that are often imperceptible in the spatial or time domain. Finally, data-driven methods focus on optimizing model architectures and refining training strategies to maximize the utility of available data [17, 23, 24, 65, 66, 69, 72].

2.2 Deformable Convolution

Standard convolution operations rely on fixed kernel shapes, which hinders their adaptability to objects exhibiting diverse structures and orientations. To address this limitation, the Deformable Convolutional Network (DCN) [5] introduces learnable offsets that dynamically adjust the kernel shape, allowing for better alignment with the target's geometry. While this innovation enhances the network's ability to model complex geometric structures, DCN faces difficulties when applied to slender shapes. To overcome this challenge, [47] proposes the Dynamic Snake Convolution (DSConv), which simulates slender structures by imposing constraints on both the initial kernel shape and the offset learning process. In 2D scenarios, for instance, it initializes with a 1D kernel oriented along a fixed coordinate axis (either x or y). The kernel points form an equidistant sequence along this primary axis. DSConv then iteratively calculates the perpendicular offsets for each kernel point, with a key constraint: the offset difference between neighboring points cannot exceed one. This design enables the representation

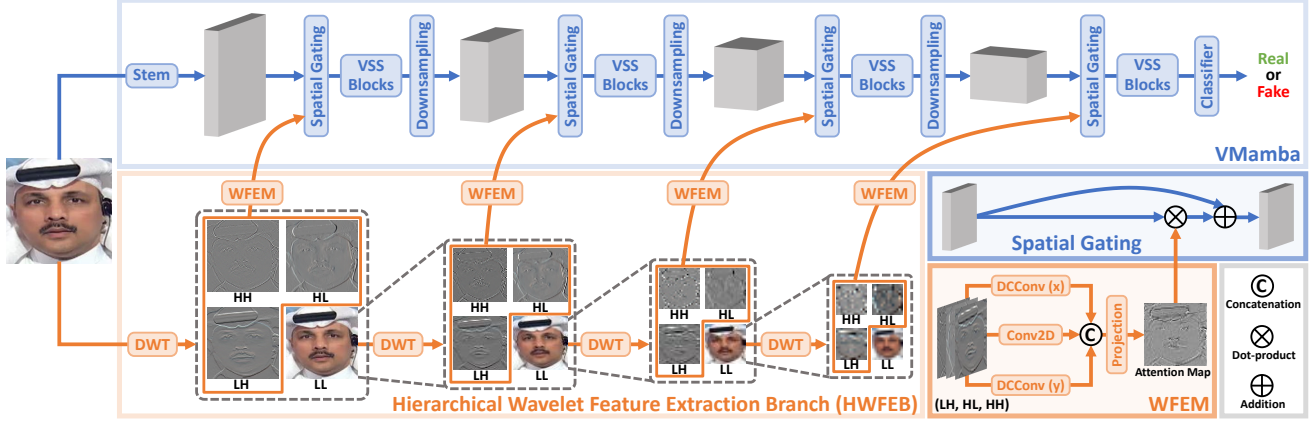


Figure 3: Overview of WMamba. The architecture comprises two main components: HWFEB and VMamba. HWFEB employs multi-level DWT to capture wavelet representations, WFEMs to generate spatial attention maps, and spatial gating mechanisms to integrate these maps into VMamba. VMamba then extracts wavelet-enhanced forgery cues and performs classification.

of slender structures with smooth and continuous topologies. However, the reliance on a predefined axis restricts DSConv’s ability to capture objects with arbitrary directions. In contrast, the proposed DCCConv dynamically learns the optimal axis orientation, allowing for the adaptation to a wider variety of slender structures. These convolutional paradigms are illustrated in Row 1 of Figure 2.

2.3 Mamba

Deep learning-driven computer vision primarily relies on CNNs and Transformers for feature extraction. While CNNs are efficient, their limited receptive fields hinder their ability to capture global context. In contrast, Transformers excel at modeling long-range relationships but suffer from quadratic computational complexity. To address this issue, **Transformer-based methods generally divide input images into large patches, which results in the loss of fine-grained spatial details.** Recently, the Mamba architecture [13], based on the SSM, has emerged as a promising alternative by achieving global perception with linear computational complexity. However, Mamba was originally designed for 1D tasks with inherent directional structures. Extending it directly to 2D vision tasks, where such directional patterns are often absent, can lead to incomplete global perception. To tackle this limitation, Vision Mamba [76] introduces a bidirectional flattening approach that flattens spatial feature maps along both positive and negative directions, resulting in a more comprehensive global perception. Building on this foundation, VMamba [35] proposes a four-directional flattening technique, enabling the discovery of richer spatial relationships. These methods are visually illustrated in Row 2 of Figure 2.

2.4 Motivation

Wavelets effectively capture key facial contours, which tend to be slender, fine-grained, and globally distributed, encoding crucial forgery clues essential for detecting manipulations, as demonstrated in Figures 1 and 4. However, existing wavelet-based detectors primarily rely on standard convolutions or Transformers for feature extraction, both of which exhibit notable limitations.

Standard convolutions struggle to capture slender structures and global context, while Transformers, although capable of modeling long-range dependencies, fail to preserve fine-grained details and delicate geometries. To address the challenge of simulating slender structures, we draw inspiration from DSConv, which constrains its initial kernel shape and offset learning process to better align with such geometries. However, DSConv’s reliance on a fixed axis significantly limits its flexibility. Therefore, we propose **DCCConv**, a novel approach that dynamically learns the optimal axis orientation, enabling robust modeling of slender structures along arbitrary directions. For capturing both fine-grained and globally distributed features, we leverage the **Mamba** architecture. Mamba achieves global perception with linear complexity, making it far more efficient than Transformers. This efficiency allows for the use of smaller image patches, facilitating the extraction of fine-grained and globally distributed characteristics. By integrating DCCConv with Mamba, the proposed WMamba fully exploits the unique properties of wavelet representations, offering a more interpretable and effective solution compared to previous wavelet-based detectors.

3 Methodology

3.1 Overview

The proposed WMamba network architecture, depicted in Figure 3, consists of two primary components: the Hierarchical Wavelet Feature Extraction Branch (HWFEB) and the VMamba model. For a given RGB input image, the HWFEB first applies a multi-level DWT to extract wavelet representations across various scales. Subsequently, these representations are processed by distinct Wavelet Feature Extraction Modules (WFEMs), which primarily leverage DCCConv to generate spatial attention maps. Next, these attention maps are seamlessly integrated into different stages of the VMamba model using spatial gating mechanisms. The model ultimately outputs two probabilities, classifying the input image as either real or fake. Since this paper focuses on the network architecture, we adopt the standard Cross-Entropy (CE) Loss function for training. The remainder of this section is organized as follows: Section 3.2

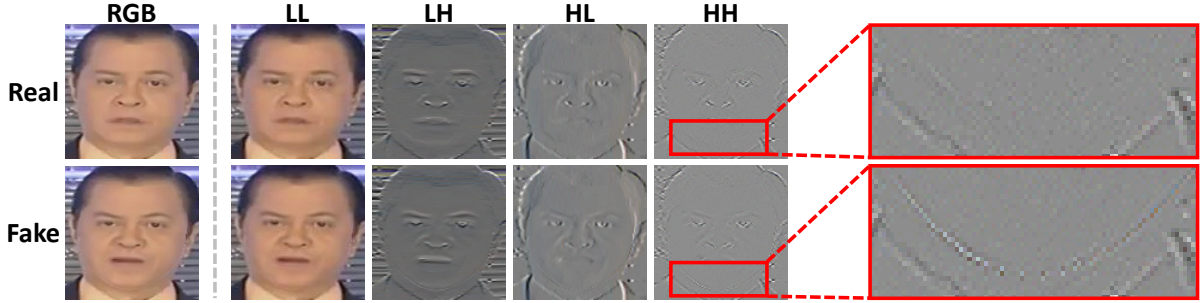


Figure 4: Visualization of different frequency sub-bands from the DWT. The LH, HL, and HH sub-bands capture high-frequency details in various orientations, while the LL sub-band represents a low-resolution approximation of the original RGB image. Highlighted within the red boxes, the high-frequency sub-bands reveal critical forgery traces that are otherwise less apparent.

provides a comprehensive description of the WMamba pipeline, while Section 3.3 offers an in-depth explanation of DCCConv.

3.2 WMamba

In this section, we will introduce the two key components of WMamba: (1) the HWFEB, which includes a multi-level DWT, multiple WFEMs, and spatial gating mechanisms, as well as (2) the VMamba model.

3.2.1 HWFEB. We begin by utilizing a **multi-level Haar DWT** to generate wavelet representations at different scales. For an input image $I \in \mathbb{R}^{H \times W \times 3}$, where H and W denote the height and width, the Haar DWT operates by convolving I with four distinct filters: f_{LL} , f_{LH} , f_{HL} , and f_{HH} . These filters correspond to the Low-Low, Low-High, High-Low, and High-High frequency sub-bands, producing the respective wavelet sub-band outputs: LL, LH, HL, and HH, each of size $\frac{H}{2} \times \frac{W}{2} \times 3$. This process can be expressed as follows:

$$\text{LL, LH, HL, HH} = (f_{LL}, f_{LH}, f_{HL}, f_{HH}) \circledast I,$$

$$f_{LL}, f_{LH}, f_{HL}, f_{HH} = \frac{1}{2} \begin{bmatrix} 1 & 1 \\ 1 & 1 \end{bmatrix}, \frac{1}{2} \begin{bmatrix} 1 & 1 \\ -1 & -1 \end{bmatrix}, \frac{1}{2} \begin{bmatrix} 1 & -1 \\ 1 & -1 \end{bmatrix}, \frac{1}{2} \begin{bmatrix} 1 & -1 \\ -1 & 1 \end{bmatrix}. \quad (1)$$

Here, \circledast represents the convolution operation. As illustrated in Figure 4, the LH, HL, and HH sub-bands capture high-frequency details, such as edges and textures, from different orientations. In contrast, the LL sub-band essentially serves as a low-resolution approximation of the input image and can be recursively decomposed. This recursive process forms a multi-level DWT, which enables the generation of wavelet representations across various scales.

Subsequently, we leverage **WFEMs** to generate spatial attention maps from the wavelet sub-bands LH, HL, and HH across multiple scales. Each WFEM extracts forgery-related features using three parallel convolutional layers: two DCCConv layers (initialized along the x-axis and y-axis, respectively) and one standard 2D convolutional layer. The DCCConv layers specialize in capturing the slender structures of facial contours, while the standard convolutional layer focuses on learning broader, more generalized patterns. The resulting feature maps from these layers are then concatenated and projected to create the desired spatial attention map.

Finally, we incorporate spatial attention maps into multiple stages of the VMamba model through **spatial gating mechanisms**. At each stage, a dot-product operation is performed to combine

the attention map with the model's feature map, enabling spatially adaptive weighting. This process effectively highlights critical features essential for identifying forgeries. In addition, we employ skip connections to enhance model stability and accelerate convergence.

HWFEB distinguishes itself from MWFEB [30] in two key aspects: (1) HWFEB exclusively uses high-frequency wavelet sub-bands, while MWFEB incorporates all wavelet components. As shown in Table 3, our selective strategy achieves superior performance. (2) HWFEB introduces the novel DCCConv to generate spatial attention maps, whereas MWFEB relies solely on standard convolutions.

3.2.2 VMamba. The Mamba architecture is based on the **SSM** [20], a foundational framework widely used in fields such as control theory, signal processing, and econometrics. The SSM transforms a 1D input signal $x(t) \in \mathbb{R}$ into a 1D output signal $y(t) \in \mathbb{R}$ through the continuous-time evolution of hidden states $h(t) \in \mathbb{R}^N$, where N represents the state dimension. This dynamic system is defined by the following set of Ordinary Differential Equations (ODEs):

$$\begin{aligned} \dot{h}(t) &= Ah(t) + Bx(t), \\ y(t) &= Ch(t) + Dx(t). \end{aligned} \quad (2)$$

Here, $A \in \mathbb{R}^{N \times N}$ is the state matrix governing the system's temporal evolution. $B \in \mathbb{R}^{N \times 1}$, $C \in \mathbb{R}^{1 \times N}$, and $D \in \mathbb{R}^{1 \times 1}$ are input, output, and feedthrough projection parameters, respectively. The system exhibits global memory characteristics, as evidenced by Equation 2, where each output depends on the entire history of past inputs through recursive state propagation. When implementing the SSM in deep learning applications, discretization is required to transform the continuous-time system into its discrete-time equivalent. This process introduces a timescale parameter $\Delta \in \mathbb{R}$, which maps the continuous-time parameters A and B to their discrete-time counterparts \bar{A} and \bar{B} . By employing the Zero-Order Hold (ZOH) algorithm, the discrete-time parameters can be calculated as follows:

$$\begin{aligned} \bar{A} &= e^{\Delta A}, \\ \bar{B} &= (\Delta A)^{-1} (e^{\Delta A} - E) \cdot \Delta B \approx \Delta B. \end{aligned} \quad (3)$$

Here, $E \in \mathbb{R}^{N \times N}$ represents the identity matrix. Then, the discrete form of Equation 2 can be expressed as follows:

$$\begin{aligned} h_t &= \bar{A}h_{t-1} + \bar{B}x_t, \\ y_t &= Ch_t + Dx_t. \end{aligned} \quad (4)$$

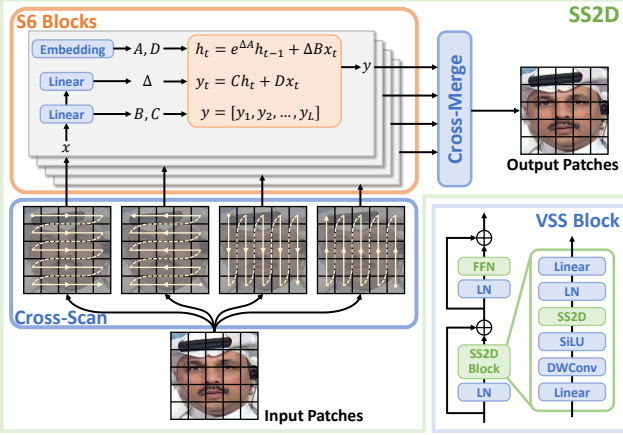


Figure 5: Schematic diagram of the VSS block, with the SS2D mechanism at its core. This mechanism flattens input image patches along four principle directions, facilitating comprehensive global perception. L denotes the number of patches.

In practice, x_t is a feature vector with multiple components, each of which is processed independently according to Equation 4.

The **WMamba** model [35], a 2D adaptation of Mamba, utilizes hierarchical Visual State Space (VSS) blocks to extract rich forgery signatures from image patches across multiple spatial resolutions. As illustrated in Figure 5, each VSS block consists of two key components: a Selective-Scan 2D (SS2D) block and a Feed Forward Network (FFN). The SS2D block performs channel projection operations and employs an SS2D mechanism to capture fine-grained, globally distributed forgery clues from input image patches. Following this, the FFN extracts channel-specific facial features, further enhancing the model's ability to learn and identify forgery artifacts.

The SS2D mechanism comprises three core components: a cross-scan module, a stack of four S6 blocks, and a cross-merge module. The cross-scan module scans input image patches along four principal directions (horizontal, vertical, and both diagonals), creating flattened sequences that effectively capture multi-directional spatial relationships. Central to the SS2D is the S6 block, a pivotal innovation introduced by Mamba [13], which integrates a selective-scan mechanism to enhance Equation 4. This mechanism dynamically learns projection and timescale parameters from the input data, thereby boosting the model's flexibility and expressiveness. Finally, the cross-merge module reconstructs the original spatial structure by unflattening the processed sequences and merging them back into a cohesive output image through fusion operations.

3.3 DCConv

Building on the work of DSConv [47], we introduce DCConv, which incorporates a learnable coordinate axis to effectively capture slender structures oriented along arbitrary directions, as demonstrated in Figure 6. Specifically, DCConv begins with a 1D convolutional kernel initially aligned along a predefined coordinate axis (either the x-axis or y-axis). For each input feature map, DCConv employs two standard 2D convolutional layers to independently generate pixel-wise offsets and rotation angles. The predicted offsets are

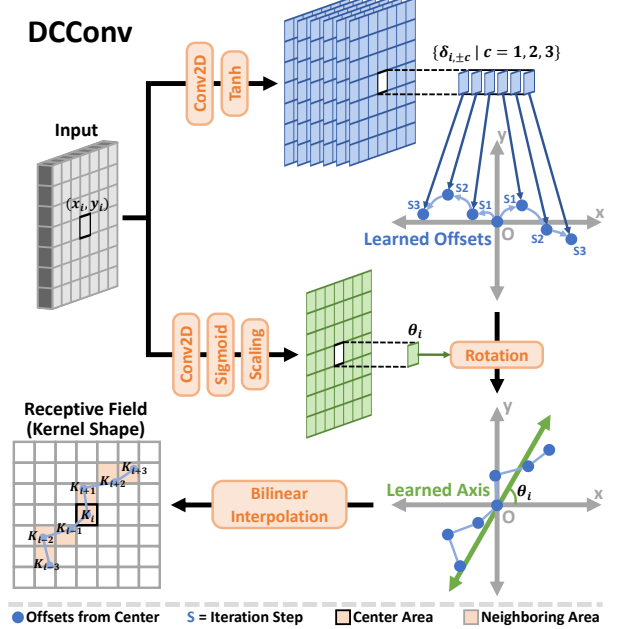


Figure 6: Schematic diagram of the proposed DCConv, initialized along the x-axis. Our method predicts both the offsets and axis orientations simultaneously, allowing for the effective representation of slender structures aligned in arbitrary directions. For illustration, the kernel length k is set to 7.

bounded within the interval $[-1, 1]$ using a Tanh activation function, while the rotation angles are constrained to the range $[0, \frac{\pi}{2}]$ through a Sigmoid activation function followed by a scaling operation. Let's consider a 1D kernel of odd length k , centered at the i -th pixel with coordinates (x_i, y_i) . The positions of the kernel points are denoted by $\{K_{i\pm c} = (x_{i\pm c}, y_{i\pm c}) \mid c = 0, 1, \dots, \frac{k-1}{2}\}$. The corresponding learned offsets for these kernel points are represented by $\{\delta_{i,\pm c} \mid c = 0, 1, \dots, \frac{k-1}{2}\}$, and the predicted rotation angle at the i -th pixel is denoted by θ_i . When the 1D kernel is initialized along the x-axis, the adjusted positions of the kernel points are computed as:

$$K_{i\pm c} = (x_i, y_i) + (\pm c, \sum_{j=0}^c \delta_{i,\pm j}) \cdot \begin{bmatrix} \cos \theta_i & \sin \theta_i \\ -\sin \theta_i & \cos \theta_i \end{bmatrix}. \quad (5)$$

In practice, the value of $\delta_{i,0}$ is set to 0, and the kernel positions are calculated iteratively in a step-by-step manner. When the 1D kernel is initialized along the y-axis, Equation 5 can be reformulated as:

$$K_{i\pm c} = (x_i, y_i) + (\sum_{j=0}^c \delta_{i,\pm j}, \pm c) \cdot \begin{bmatrix} \cos \theta_i & \sin \theta_i \\ -\sin \theta_i & \cos \theta_i \end{bmatrix}. \quad (6)$$

The combination of the Tanh activation function and the iterative calculation process ensures that the offset differences between adjacent kernel points remain consistently below one, facilitating the effective extraction of slender structures with smooth and continuous topologies. **Furthermore, the learned rotation angles enable DCConv to theoretically model slender structures oriented in any direction.** This flexibility allows DCConv to capture a wider range of slender geometries compared to DSConv, which

Table 1: Cross-dataset evaluation of representative face forgery detection methods on the CDF, DFDC, DFDCP, and FFIW datasets. Methods marked with the symbol * are reproduced using the official codes, while results for other methods are taken directly from their respective papers. The best performance is highlighted in BOLD, and the second best is underlined. Notably, WMamba achieves SOTA performance across all datasets, demonstrating exceptional generalization capability.

Method	Venue	Input Type	Training Set		Test Set AUC (%)			
			Real	Fake	CDF	DFDC	DFDCP	FFIW
F ³ -Net* [48]	ECCV 2020	Frame	✓	✓	77.92	67.35	73.54	70.11
LTW* [56]	AAAI 2021	Frame	✓	✓	77.14	69.00	74.58	76.63
PCL+I2G [72]	ICCV 2021	Frame	✓		90.03	67.52	74.37	-
DCL [57]	AAAI 2022	Frame	✓	✓	82.30	-	76.71	71.14
SBI [52]	CVPR 2022	Frame	✓		93.18	72.42	86.15	84.83
F ² Trans [40]	TIFS 2023	Frame	✓	✓	89.87	-	76.15	-
SeeABLE [28]	ICCV 2023	Frame	✓		87.30	75.90	86.30	-
AUNet [1]	CVPR 2023	Frame	✓		92.77	73.82	86.16	81.45
LAA-Net [42]	CVPR 2024	Frame	✓		95.40	-	86.94	-
RAE [61]	ECCV 2024	Frame	✓		<u>95.50</u>	80.20	<u>89.50</u>	-
FreqBlender [74]	NeurIPS 2024	Frame	✓		94.59	74.59	87.56	<u>86.14</u>
UDD [12]	AAAI 2025	Frame	✓	✓	93.10	<u>81.20</u>	88.10	-
LESB [54]	WACVW 2025	Frame	✓		93.13	71.98	-	83.01
FTCN* [73]	ICCV 2021	Video	✓	✓	86.90	71.00	74.00	74.47
RealForensics [18]	CVPR 2022	Video	✓	✓	86.90	-	75.90	-
TALL [63]	ICCV 2023	Video	✓	✓	90.79	-	76.78	-
TALL++ [64]	IJCV 2024	Video	✓	✓	91.96	-	78.51	-
NACO [70]	ECCV 2024	Video	✓	✓	89.50	-	76.70	-
WMamba (Ours)	-	Frame	✓		96.29	82.97	89.62	86.59

can be regarded as a special case of DCConv when $\theta_i = 0$. A visual comparison of these two convolutional paradigms are provided in Appendix A. Since the offsets are typically fractional, bilinear interpolation is used to compute the receptive field values (*i.e.*, to sample the input feature map) during the convolution operation, as described in [5].

4 Experiments

4.1 Setup

4.1.1 Datasets. For training, we utilize the widely recognized FaceForensics++ (FF++) [50] benchmark dataset, which comprises 1,000 authentic face videos and 4,000 manipulated videos generated using four distinct forgery techniques: DeepFakes (DF), Face2Face (F2F) [60], FaceSwap (FS), and NeuralTextures (NT) [59]. Notably, this study leverages the SBI framework [52], enabling our model to be trained exclusively on real face videos. This approach supports cross-manipulation evaluation across all four forgery types in FF++. To assess cross-dataset generalizability, we test our model on four popular datasets: Celeb-DeepFake-v2 (CDF) [32], which employs advanced deepfake methods on YouTube celebrity content; the DeepFake Detection Challenge (DFDC) [8] and its Preview version (DFDCP) [9], which feature videos with various perturbations including compression, downsampling, and noise; and FFIW-10K (FFIW) [75], which adds complexity with multi-person scenarios.

4.1.2 Frame-Level Baselines. We evaluate our approach against thirteen SOTA frame-level baselines for face forgery detection, each employing distinct strategies. F³-Net [48] leverages frequency-aware manipulation clues, while LTW [56] emphasizes domain-general detection. PCL+I2G [72] focuses on source feature inconsistencies, and DCL [57] employs multi-granular contrastive learning. SBI [52] enhances training by generating synthetic fake faces, and F²Trans [40] integrates spatial and frequency domain forgery traces. SeeABLE [28] reformulates forgery detection as an Out-Of-Distribution (OOD) problem, while AUNet [1] explores facial Action Unit (AU) regions for more nuanced analysis. LAA-Net [42] incorporates heatmap-guided self-consistency attention, and RAE [61] aims to recover real facial appearances from perturbations. FreqBlender [74] synthesizes pseudo-fake faces by blending frequency knowledge, UDD [12] addresses position and content biases with a dual-branch architecture, and LESB [54] introduces a Local Feature Discovery (LFD) technique to produce self-blended samples.

4.1.3 Video-Level Baselines. We further compare our method with five video-level face forgery detection approaches. These include FTCN [73], which exploits temporal coherence patterns; RealForensics [18], which employs a two-stage framework trained on natural talking face datasets; TALL [63], which preserves spatio-temporal dependencies through layout transformation; the enhanced version TALL++ [64], which incorporates a Graph Reasoning Block (GRB)

Table 2: Cross-manipulation evaluation of methods trained only on real face videos from FF++. Notably, our method delivers the best results across all tested manipulations.

Method	Test Set AUC (%)				
	DF	F2F	FS	NT	FF++
PCL+I2G [72]	100	98.97	99.86	97.63	99.11
SBI [52]	<u>99.99</u>	<u>99.88</u>	<u>99.91</u>	<u>98.79</u>	<u>99.64</u>
SeeABLE [28]	99.20	98.80	99.10	96.90	98.50
AUNet [1]	99.98	99.60	99.89	98.38	99.46
RAE [61]	99.60	99.10	99.20	97.60	98.90
WMamba	100	99.98	99.94	98.88	99.70

Table 3: Ablation study results on the structure of HWFEB.

Method	Test Set AUC (%)			
	CDF	DFDC	DFDCP	FFIW
w/ LL	<u>95.61</u>	80.25	87.47	85.68
w/o Hierarchical	94.76	<u>81.79</u>	<u>87.88</u>	85.03
w/ Addition	94.70	77.57	87.13	<u>86.34</u>
w/ Concatenation	84.54	69.19	78.22	65.05
w/o Skip Connection	95.14	78.51	85.75	84.61
The Proposed	96.29	82.97	89.62	86.59

and Semantic Consistency (SC) loss; and NACO [70], which learns natural consistency representations from authentic face videos.

4.1.4 Evaluation Metric. We evaluate the detection performance of various methods using the Area Under the Receiver Operating Characteristic Curve (AUC), a standard metric in face forgery detection. For frame-level methods, we report video-level results, which average the predictions across all frames within each video, allowing for a fair and direct comparison with video-level approaches.

4.1.5 Implementation Details. This work leverages the synthetic data generation framework, preprocessing techniques, and data augmentation strategies introduced by SBI [52]. For further details, please refer to Appendix B. We adopt VMamba-S [35] as our backbone network, which consists of 2, 2, 15, and 2 VSS blocks across its four stages. The network is pre-trained on the ImageNet-1K dataset [6], providing a strong initialization. In addition, we configure DCCConv with a kernel length of 9. The WMamba model is trained using the AdamW optimizer [38] with a batch size of 64 and an initial learning rate of 5e-5. Training spans 200 epochs, during which the learning rate is linearly decayed starting from the 100th epoch to facilitate smoother convergence. All experiments are implemented in PyTorch, and training WMamba under these configurations requires approximately 30 GB of GPU memory.

4.2 Results

4.2.1 Cross-Dataset Evaluation. Cross-dataset evaluation is a crucial testing protocol for face forgery detection, as it measures a

Table 4: Ablation study results for DCCConv, showcasing its superiority over other deformable convolution paradigms.

Method	Test Set AUC (%)			
	CDF	DFDC	DFDCP	FFIW
w/ DCN [5]	95.15	80.15	<u>87.77</u>	85.53
w/ DCN-v2 [77]	95.25	80.96	86.74	85.59
w/ DSConv [47]	94.42	<u>82.87</u>	85.83	<u>86.26</u>
w/o DCCConv	<u>96.06</u>	80.24	87.21	85.88
The Proposed	96.29	82.97	89.62	86.59

Table 5: Comparison of different VMamba backbones.

Backbone	Params	Test Set AUC (%)				
		CDF	DFDC	DFDCP	FFIW	Avg.
VMamba-T	30M	<u>95.82</u>	<u>82.00</u>	<u>88.03</u>	83.15	87.25
VMamba-S	50M	96.29	82.97	89.62	<u>86.59</u>	88.87
VMamba-B	89M	95.29	81.64	88.09	87.29	<u>88.08</u>

model’s ability to generalize to unseen data. In Table 1, we compare our method against recent SOTA approaches. The proposed WMamba achieves the highest AUC scores across all unseen datasets, demonstrating its exceptional generalization capability. This superior performance can be attributed to the synergistic effectiveness of DCCConv and VMamba, which fully leverage wavelet information to facilitate the comprehensive extraction of forgery clues.

4.2.2 Cross-Manipulation Evaluation. In practice, defenders are often unaware of the exact forgery techniques used by attackers. Therefore, it is crucial to assess a model’s ability to generalize across various types of manipulations. Following the protocol outlined in [52], we compare our method with approaches trained exclusively on real face videos from FF++. The results, shown in Table 2, highlight WMamba’s effectiveness in handling unseen manipulations.

4.3 Ablation Studies

In this section, we present extensive ablation study results on HWFEB, DCCConv, and VMamba. We also include visual demonstrations to highlight the efficacy of HWFEB and DCCConv. Additional findings from our ablation studies are provided in Appendix C.

4.3.1 Structural Analysis of the HWFEB. We validate the design choices of HWFEB through comprehensive ablation studies conducted on five architectural variants. Specifically, our experiments investigate: (1) the impact of including the LL component in WFEMs (w/ LL), compared to our baseline using only LH, HL, and HH subbands for wavelet guidance; (2) the benefits of employing multi-scale wavelet representations over single-scale analysis (w/o Hierarchical); and (3) the effectiveness of the spatial gating mechanism versus alternative feature fusion strategies (w/ Addition, w/ Concatenation, and w/o Skip Connection). The cross-dataset evaluation results, presented in Table 3, validate our design decisions by demonstrating superior performance across all tested variants.

Table 6: Performance and efficiency analysis of popular network architectures with and without HWFEB. ViT extracts features at a single scale, which makes it incompatible with HWFEB. We report the token numbers at the first stage of each network. Notably, VMamba outperforms both the CNN-based ConvNeXt and Transformer-based ViT and Swin. Additionally, VMamba showcases significantly better efficiency than ViT. Furthermore, integrating HWFEB consistently improves detection performance across all backbones.

Method	Params	FLOPs	Tokens	Test Set AUC (%)				
				CDF	DFDC	DFDCP	FFIW	
ConvNeXt-S	50M	8.7G	3,136	94.39	80.23	86.26	82.04	
	51M	8.9G	3,136	94.46	<u>82.17</u>	86.22	84.60	
ViT-B/16	86M	17.6G	197	93.64	79.66	85.73	83.92	
Swin-S	50M	8.7G	3,136	95.26	80.06	86.80	84.87	
	51M	8.9G	3,136	95.60	81.01	<u>87.91</u>	<u>86.33</u>	
VMamba-S	50M	8.7G	3,136	95.39	81.37	86.93	85.60	
	51M	8.9G	3,136	96.29	82.97	89.62	86.59	

4.3.2 Effectiveness of DCConv. To validate the efficacy of DCConv, we conduct comparative experiments against DCN [5], DCN-v2 [77], DSConv [47], and a baseline network without DCConv. The cross-dataset evaluation results, shown in Table 4, **clearly demonstrate that DCConv consistently outperforms other deformable convolution paradigms**, underscoring its superior capability to capture the slender structures of facial contours.

4.3.3 Analysis of VMamba. We systematically evaluate three versions of the VMamba backbone, namely VMamba-T (Tiny), VMamba-S (Small), and VMamba-B (Base). The cross-dataset assessment results, as presented in Table 5, challenge the conventional assumption that larger architectures inherently deliver better performance. We conjecture that the greater capacity of VMamba-B leads to overfitting on the training set, consequently hindering its generalization to new, unseen examples. Notably, VMamba-S demonstrates superior performance compared to both its smaller and larger counterparts, establishing it as the optimal backbone for WMamba.

Furthermore, we compare VMamba against three widely used network architectures: the CNN-based ConvNeXt [37] and the Transformer-based ViT [11] and Swin [36]. ViT processes features at a fixed 14×14 spatial resolution, whereas other architectures adopt a hierarchical design, extracting features across multiple scales (up to 56×56). Adapting ViT to support multi-scale feature extraction would drastically increase its computational cost by two orders of magnitude, making it impractical. Although Swin improves efficiency through windowed attention, this localized approach limits its ability to capture long-range spatial relationships. For a fair comparison, all backbones are pre-trained on ImageNet-1K and matched in parameter count. The cross-dataset evaluation results presented in Table 6 reveal three insights: (1) **VMamba outperforms both CNN- and Transformer-based architectures, highlighting its superior capability in face forgery detection;** (2) **VMamba achieves comparable computational efficiency to ConvNeXt**

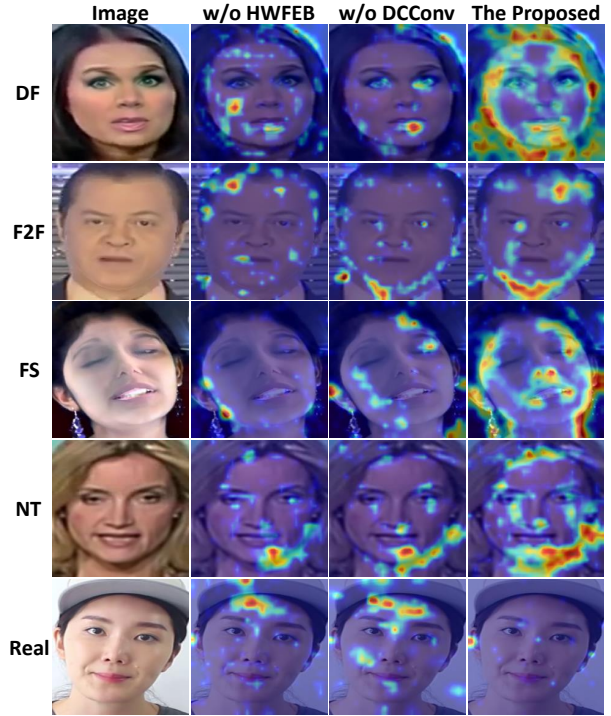


Figure 7: Saliency maps on four distinct manipulated samples and one real sample from the FF++ dataset. For the forged instances, HWFEB and DCConv guide our model’s attention to key facial contours that are rich in forgery artifacts.

and Swin in terms of FLOPs and token counts, while significantly surpassing ViT in this regard; and (3) incorporating the HWFEB consistently enhances detection performance, demonstrating its effectiveness as a plug-and-play module.

4.3.4 Visual Analysis of HWFEB & DCConv. We further validate the effectiveness of HWFEB and DCConv using Grad-CAM visualizations [51], which highlight the spatial regions most critical to the model’s decision-making process. The saliency maps in Figure 7 indicate that, for fake samples, HWFEB and DCConv direct the model’s attention to key facial contours rich in forgery artifacts. In contrast, for the real sample, our model exhibits minimal activation.

5 Conclusion

In this paper, we propose WMamba, a wavelet-based feature extractor built upon the Mamba architecture. WMamba fully considers the slender, fine-grained, and globally distributed nature of facial contours, maximizing the utility of wavelet data via two key innovations. First, we introduce DCConv, which employs a learnable coordinate axis to capture a broader range of slender structures. Second, by leveraging the Mamba architecture, which excels at modeling long-range spatial dependencies with linear complexity, WMamba effectively captures fine-grained, globally distributed forgery clues from small image patches. Our method achieves SOTA performance in both cross-dataset and cross-manipulation evaluations, demonstrating its effectiveness in face forgery detection.

Acknowledgments

This work was supported in part by Chinese National Natural Science Foundation Projects U23B2054, 62276254, 62306313, the Beijing Science and Technology Plan Project Z231100005923033, Beijing Natural Science Foundation L221013, the Science and Technology Development Fund of Macau Project 0140/2024/AGJ, and InnoHK program.

References

- [1] Weiming Bai, Yufan Liu, Zhipeng Zhang, Bing Li, and Weiming Hu. 2023. AUNet: Learning Relations Between Action Units for Face Forgery Detection. In *Proceedings of the IEEE/CVF Conference on Computer Vision and Pattern Recognition (CVPR)*. 24709–24719.
- [2] Alexander Buslaev, Vladimir I Iglovikov, Eugene Khvedchenya, Alex Parinov, Mikhail Druzhinin, and Alexandra A Kalinin. 2020. Albumentations: fast and flexible image augmentations. *Information* 11, 2 (2020), 125.
- [3] Junyi Cao, Chao Ma, Taiping Yao, Shen Chen, Shouhong Ding, and Xiaokang Yang. 2022. End-to-End Reconstruction-Classification Learning for Face Forgery Detection. In *Proceedings of the IEEE/CVF Conference on Computer Vision and Pattern Recognition (CVPR)*. 4113–4122.
- [4] Xinjie Cui, Yuezun Li, Ao Luo, Jiaran Zhou, and Junyu Dong. 2024. Forensics Adapter: Adapting CLIP for Generalizable Face Forgery Detection. *arXiv preprint arXiv:2411.19715* (2024).
- [5] Jifeng Dai, Haizhi Qi, Yuwen Xiong, Yi Li, Guodong Zhang, Han Hu, and Yichen Wei. 2017. Deformable Convolutional Networks. In *Proceedings of the IEEE International Conference on Computer Vision (ICCV)*.
- [6] Jia Deng, Wei Dong, Richard Socher, Li-Jia Li, Kai Li, and Li Fei-Fei. 2009. ImageNet: A large-scale hierarchical image database. In *2009 IEEE Conference on Computer Vision and Pattern Recognition (CVPR)*. 248–255.
- [7] Jiankang Deng, Jia Guo, Evangelos Ververas, Irene Kotsia, and Stefanos Zafeiriou. 2020. RetinaFace: Single-Shot Multi-Level Face Localisation in the Wild. In *Proceedings of the IEEE/CVF Conference on Computer Vision and Pattern Recognition (CVPR)*.
- [8] Brian Dolhansky, Joanna Bitton, Ben Pflaum, Jikuo Lu, Russ Howes, Menglin Wang, and Cristian Canton Ferrer. 2020. The deepfake detection challenge (dfdc) dataset. *arXiv preprint arXiv:2006.07397* (2020).
- [9] Brian Dolhansky, Russ Howes, Ben Pflaum, Nicole Baram, and Cristian Canton Ferrer. 2019. The deepfake detection challenge (dfdc) preview dataset. *arXiv preprint arXiv:1910.08854* (2019).
- [10] Alexey Dosovitskiy, Lucas Beyer, Alexander Kolesnikov, Dirk Weissenborn, Xiaohua Zhai, Thomas Unterthiner, Mostafa Dehghani, Matthias Minderer, Georg Heigold, Sylvain Gelly, et al. 2020. An image is worth 16x16 words: Transformers for image recognition at scale. *arXiv preprint arXiv:2010.11929* (2020).
- [11] Alexey Dosovitskiy, Lucas Beyer, Alexander Kolesnikov, Dirk Weissenborn, Xiaohua Zhai, Thomas Unterthiner, Mostafa Dehghani, Matthias Minderer, Georg Heigold, Sylvain Gelly, Jakob Uszkoreit, and Neil Houlsby. 2021. An Image is Worth 16x16 Words: Transformers for Image Recognition at Scale. In *International Conference on Learning Representation (ICLR)*.
- [12] Xinghe Fu, Zhiyuan Yan, Taiping Yao, Shen Chen, and Xi Li. 2025. Exploring Unbiased Deepfake Detection via Token-Level Shuffling and Mixing. In *Proceedings of the AAAI Conference on Artificial Intelligence (AAAI)*.
- [13] Albert Gu and Tri Dao. 2023. Mamba: Linear-time sequence modeling with selective state spaces. *arXiv preprint arXiv:2312.00752* (2023).
- [14] Zhihao Gu, Yang Chen, Taiping Yao, Shouhong Ding, Jilin Li, Feiyue Huang, and Lizhuang Ma. 2021. Spatiotemporal Inconsistency Learning for DeepFake Video Detection. In *Proceedings of the 29th ACM International Conference on Multimedia (ACM MM)*. 3473–3481.
- [15] Zhihao Gu, Yang Chen, Taiping Yao, Shouhong Ding, Jilin Li, and Lizhuang Ma. 2022. Delving into the local: Dynamic inconsistency learning for deepfake video detection. In *Proceedings of the AAAI conference on artificial intelligence (AAAI)*, Vol. 36. 744–752.
- [16] Zhihao Gu, Taiping Yao, Yang Chen, Shouhong Ding, and Lizhuang Ma. 2022. Hierarchical contrastive inconsistency learning for deepfake video detection. In *Proceedings of The 17th European conference on computer vision (ECCV)*. Springer, 596–613.
- [17] Xiao Guo, Xiaohong Liu, Zhiyuan Ren, Steven Grossz, Iacopo Masi, and Xiaoming Liu. 2023. Hierarchical Fine-Grained Image Forgery Detection and Localization. In *Proceedings of the IEEE/CVF Conference on Computer Vision and Pattern Recognition (CVPR)*. 3155–3165.
- [18] Alexandros Haliassos, Rodrigo Mira, Stavros Petridis, and Maja Pantic. 2022. Leveraging Real Talking Faces via Self-Supervision for Robust Forgery Detection. In *Proceedings of the IEEE/CVF Conference on Computer Vision and Pattern Recognition (CVPR)*. 14950–14962.
- [19] Alexandros Haliassos, Konstantinos Vougioukas, Stavros Petridis, and Maja Pantic. 2021. Lips Don't Lie: A Generalisable and Robust Approach To Face Forgery Detection. In *Proceedings of the IEEE/CVF Conference on Computer Vision and Pattern Recognition (CVPR)*. 5039–5049.
- [20] James D. Hamilton. 1994. Chapter 50 State-space models. *Handbook of Econometrics*, Vol. 4. Elsevier, 3039–3080.
- [21] Peisong He, Haoliang Li, and Hongxia Wang. 2019. Detection of Fake Images Via The Ensemble of Deep Representations from Multi Color Spaces. In *2019 IEEE International Conference on Image Processing (ICIP)*. 2299–2303.
- [22] Gee-Sern Hsu, Chun-Hung Tsai, and Hung-Yi Wu. 2022. Dual-Generator Face Reenactment. In *Proceedings of the IEEE/CVF Conference on Computer Vision and Pattern Recognition (CVPR)*. 642–650.
- [23] Juan Hu, Xin Liao, Jinwen Liang, Wenbo Zhou, and Zheng Qin. 2022. Finfer: Frame inference-based deepfake detection for high-visual-quality videos. In *Proceedings of the AAAI conference on artificial intelligence (AAAI)*, Vol. 36. 951–959.
- [24] Baojin Huang, Zhongyuan Wang, Jifan Yang, Jiaxin Ai, Qin Zou, Qian Wang, and Dengpan Ye. 2023. Implicit Identity Driven Deepfake Face Swapping Detection. In *Proceedings of the IEEE/CVF Conference on Computer Vision and Pattern Recognition (CVPR)*. 4490–4499.
- [25] Gengyun Jia, Meisong Zheng, Chuanrui Hu, Xin Ma, Yuting Xu, Luoqi Liu, Yafeng Deng, and Ran He. 2021. Inconsistency-Aware Wavelet Dual-Branch Network for Face Forgery Detection. *IEEE Transactions on Biometrics, Behavior, and Identity Science* 3, 3 (2021), 308–319.
- [26] Davis E King. 2009. Dlib-ml: A machine learning toolkit. *The Journal of Machine Learning Research* 10 (2009), 1755–1758.
- [27] Mohammad Rami Koujan, Michail Christos Doukas, Anastasios Roussos, and Stefanos Zafeiriou. 2020. Head2Head: Video-based Neural Head Synthesis. In *2020 15th IEEE International Conference on Automatic Face and Gesture Recognition (FG 2020)*. 16–23.
- [28] Nicolas Larue, Ngoc-Son Vu, Vitomir Struc, Peter Peer, and Vassilis Christophides. 2023. SeeABLE: Soft Discrepancies and Bounded Contrastive Learning for Exposing Deepfakes. In *Proceedings of the IEEE/CVF International Conference on Computer Vision (ICCV)*. 21011–21021.
- [29] Jiaming Li, Hongtao Xie, Jiahong Li, Zhongyuan Wang, and Yongdong Zhang. 2021. Frequency-Aware Discriminative Feature Learning Supervised by Single-Center Loss for Face Forgery Detection. In *Proceedings of the IEEE/CVF Conference on Computer Vision and Pattern Recognition (CVPR)*. 6458–6467.
- [30] Jiaming Li, Hongtao Xie, Lingyun Yu, and Yongdong Zhang. 2022. Wavelet-enhanced Weakly Supervised Local Feature Learning for Face Forgery Detection. In *Proceedings of the 30th ACM International Conference on Multimedia (ACM MM)*. 1299–1308.
- [31] Lingzhi Li, Jianmin Bao, Hao Yang, Dong Chen, and Fang Wen. 2019. Faceshifter: Towards high fidelity and occlusion aware face swapping. *arXiv preprint arXiv:1912.13457* (2019).
- [32] Yuezun Li, Xin Yang, Pu Sun, Honggang Qi, and Siwei Lyu. 2020. Celeb-DF: A Large-Scale Challenging Dataset for DeepFake Forensics. In *Proceedings of the IEEE/CVF Conference on Computer Vision and Pattern Recognition (CVPR)*.
- [33] Tsung-Yi Lin, Priya Goyal, Ross Girshick, Kaiming He, and Piotr Dollar. 2017. Focal Loss for Dense Object Detection. In *Proceedings of the IEEE International Conference on Computer Vision (ICCV)*.
- [34] Jie Liu, Jingjing Wang, Peng Zhang, Chunmao Wang, Di Xie, and Shiliang Pu. 2022. Multi-Scale Wavelet Transformer for Face Forgery Detection. In *Proceedings of the Asian Conference on Computer Vision (ACCV)*. 1858–1874.
- [35] Yue Liu, Yunjie Tian, Yuzhong Zhao, Hongtian Yu, Lingxi Xie, Yaowei Wang, Qixiang Ye, Jianbin Jiao, and Yunfan Liu. 2024. VMamba: Visual State Space Model. In *Advances in Neural Information Processing Systems (NeurIPS)*, Vol. 37. 103031–103063.
- [36] Ze Liu, Yutong Lin, Yue Cao, Han Hu, Yixuan Wei, Zheng Zhang, Stephen Lin, and Baining Guo. 2021. Swin Transformer: Hierarchical Vision Transformer Using Shifted Windows. In *Proceedings of the IEEE/CVF International Conference on Computer Vision (ICCV)*. 10012–10022.
- [37] Zhuang Liu, Hanzi Mao, Chao-Yuan Wu, Christoph Feichtenhofer, Trevor Darrell, and Saining Xie. 2022. A ConvNet for the 2020s. In *Proceedings of the IEEE/CVF Conference on Computer Vision and Pattern Recognition (CVPR)*. 11976–11986.
- [38] Ilya Loshchilov and Frank Hutter. 2017. Decoupled Weight Decay Regularization. *arXiv preprint arXiv:1711.05101* (2017).
- [39] Scott McCloskey and Michael Albright. 2019. Detecting GAN-Generated Imagery Using Saturation Cues. In *2019 IEEE International Conference on Image Processing (ICIP)*. 4584–4588.
- [40] Changtao Miao, Zichang Tan, Qi Chu, Huan Liu, Honggang Hu, and Nenghai Yu. 2023. F2Trans: High-Frequency Fine-Grained Transformer for Face Forgery Detection. *IEEE Transactions on Information Forensics and Security* 18 (2023), 1039–1051.
- [41] Fausto Milletari, Nassir Navab, and Seyed-Ahmad Ahmadi. 2016. V-net: Fully convolutional neural networks for volumetric medical image segmentation. In *2016 Fourth International Conference on 3D Vision (3DV)*. Ieee, 565–571.
- [42] Dat Nguyen, Nesryne Mejri, Inder Pal Singh, Polina Kuleshova, Marcella Astrid, Anis Kacem, Enjie Ghorbel, and Djamilia Aouada. 2024. LAA-Net: Localized Artifact Attention Network for Quality-Agnostic and Generalizable Deepfake

Detection. In *Proceedings of the IEEE/CVF Conference on Computer Vision and Pattern Recognition (CVPR)*. 17395–17405.

[43] Yuval Nirkin, Yosi Keller, and Tal Hassner. 2019. FSGAN: Subject Agnostic Face Swapping and Reenactment. In *Proceedings of the IEEE/CVF International Conference on Computer Vision (ICCV)*. 7184–7193.

[44] Jinyoung Park, Sungdong Yoo, Jihwan Park, and Hyunwoo J Kim. 2022. Deformable graph convolutional networks. In *Proceedings of the AAAI Conference on Artificial Intelligence (AAAI)*, Vol. 36. 7949–7956.

[45] Gan Pei, Jiangning Zhang, Menghan Hu, Zhenyu Zhang, Chengjie Wang, Yunsheng Wu, Guangtao Zhai, Jian Yang, Chunhua Shen, and Dacheng Tao. 2024. Deepfake generation and detection: A benchmark and survey. *arXiv preprint arXiv:2403.17881* (2024).

[46] Chunlei Peng, Zimin Miao, Decheng Liu, Nannan Wang, Ruimin Hu, and Xinbo Gao. 2024. Where Deepfakes Gaze at? Spatial-Temporal Gaze Inconsistency Analysis for Video Face Forgery Detection. *IEEE Transactions on Information Forensics and Security* 19 (2024), 4507–4517.

[47] Yaolei Qi, Yuting He, Xiaoming Qi, Yuan Zhang, and Guanyu Yang. 2023. Dynamic Snake Convolution Based on Topological Geometric Constraints for Tubular Structure Segmentation. In *Proceedings of the IEEE/CVF International Conference on Computer Vision (ICCV)*. 6070–6079.

[48] Yuyang Qian, Guojun Yin, Lu Sheng, Zixuan Chen, and Jing Shao. 2020. Thinking in frequency: Face forgery detection by mining frequency-aware clues. In *Proceedings of The 16th European conference on computer vision (ECCV)*. Springer, 86–103.

[49] Olaf Ronneberger, Philipp Fischer, and Thomas Brox. 2015. U-net: Convolutional networks for biomedical image segmentation. In *International Conference on Medical Image Computing and Computer Assisted Intervention (MICCAI)*. Springer, 234–241.

[50] Andreas Rossler, Davide Cozzolino, Luisa Verdoliva, Christian Riess, Justus Thies, and Matthias Niessner. 2019. FaceForensics++: Learning to Detect Manipulated Facial Images. In *Proceedings of the IEEE/CVF International Conference on Computer Vision (ICCV)*.

[51] Ramprasaath R. Selvaraju, Michael Cogswell, Abhishek Das, Ramakrishna Vedantam, Devi Parikh, and Dhruv Batra. 2017. Grad-CAM: Visual Explanations From Deep Networks via Gradient-Based Localization. In *Proceedings of the IEEE International Conference on Computer Vision (ICCV)*.

[52] Kaede Shiohara and Toshihiko Yamasaki. 2022. Detecting Deepfakes With Self-Blended Images. In *Proceedings of the IEEE/CVF Conference on Computer Vision and Pattern Recognition (CVPR)*. 18720–18729.

[53] Kaede Shiohara, Xingchao Yang, and Takafumi Taketomi. 2023. BlendFace: Re-designing Identity Encoders for Face-Swapping. In *Proceedings of the IEEE/CVF International Conference on Computer Vision (ICCV)*. 7634–7644.

[54] Elahe Soltandoost, Richard Plesh, Stephanie Schuckers, Peter Peer, and Vito-mir Štruc. 2025. Extracting Local Information from Global Representations for Interpretable Deepfake Detection. In *Proceedings of the Winter Conference on Applications of Computer Vision (WACV) Workshops*. 1629–1639.

[55] J. Staal, M.D. Abramoff, M. Niemeijer, M.A. Viergever, and B. van Ginneken. 2004. Ridge-based vessel segmentation in color images of the retina. *IEEE Transactions on Medical Imaging* 23, 4 (2004), 501–509.

[56] Ke Sun, Hong Liu, Qixiang Ye, Yue Gao, Jianzhuang Liu, Ling Shao, and Rongrong Ji. 2021. Domain general face forgery detection by learning to weight. In *Proceedings of the AAAI conference on artificial intelligence (AAAI)*, Vol. 35. 2638–2646.

[57] Ke Sun, Taiping Yao, Shen Chen, Shouhong Ding, Jilin Li, and Rongrong Ji. 2022. Dual contrastive learning for general face forgery detection. In *Proceedings of the AAAI Conference on Artificial Intelligence (AAAI)*, Vol. 36. 2316–2324.

[58] Chuangchuang Tan, Yao Zhao, Shikui Wei, Guanghua Gu, Ping Liu, and Yunchao Wei. 2024. Frequency-aware deepfake detection: Improving generalizability through frequency space domain learning. In *Proceedings of the AAAI Conference on Artificial Intelligence (AAAI)*, Vol. 38. 5052–5060.

[59] Justus Thies, Michael Zollhöfer, and Matthias Nießner. 2019. Deferred neural rendering: Image synthesis using neural textures. *ACM Transactions on Graphics* 38, 4 (2019), 1–12.

[60] Justus Thies, Michael Zollhöfer, Marc Stamminger, Christian Theobalt, and Matthias Niessner. 2016. Face2Face: Real-Time Face Capture and Reenactment of RGB Videos. In *Proceedings of the IEEE Conference on Computer Vision and Pattern Recognition (CVPR)*.

[61] Jiahe Tian, Cai Yu, Xi Wang, Peng Chen, Zihao Xiao, Jiao Dai, Jizhong Han, and Yesheng Chai. 2024. Real Appearance Modeling for More General Deepfake Detection. In *Proceedings of The 18th European Conference on Computer Vision (ECCV)*. 402–419.

[62] Sifan Wu, Haipeng Chen, Yifang Yin, Sihao Hu, Runyang Feng, Yingying Jiao, Ziqi Yang, and Zhenguang Liu. 2024. Joint-Motion Mutual Learning for Pose Estimation in Video. In *Proceedings of the 32nd ACM International Conference on Multimedia (ACM MM)*. 8962–8971.

[63] Yuting Xu, Jian Liang, Gengyun Jia, Ziming Yang, Yanhao Zhang, and Ran He. 2023. TALL: Thumbnail Layout for Deepfake Video Detection. In *Proceedings of the IEEE/CVF International Conference on Computer Vision (ICCV)*. 22658–22668.

[64] Yuting Xu, Jian Liang, Lijun Sheng, and Xiao-Yu Zhang. 2024. Towards Generalizable Deepfake Video Detection with Thumbnail Layout and Graph Reasoning. *arXiv preprint arXiv:2403.10261* (2024).

[65] Zhiyuan Yan, Yuhao Luo, Siwei Lyu, Qingshan Liu, and Baoyuan Wu. 2024. Transcending Forgery Specificity with Latent Space Augmentation for Generalizable Deepfake Detection. In *Proceedings of the IEEE/CVF Conference on Computer Vision and Pattern Recognition (CVPR)*. 8984–8994.

[66] Zhiyuan Yan, Yong Zhang, Yanbo Fan, and Baoyuan Wu. 2023. UCF: Uncovering Common Features for Generalizable Deepfake Detection. In *Proceedings of the IEEE/CVF International Conference on Computer Vision (ICCV)*. 22412–22423.

[67] Ziming Yang, Jian Liang, Yuting Xu, Xiao-Yu Zhang, and Ran He. 2023. Masked Relation Learning for DeepFake Detection. *IEEE Transactions on Information Forensics and Security* 18 (2023), 1696–1708.

[68] Peipeng Yu, Jianwei Fei, Zhihua Xia, Zhili Zhou, and Jian Weng. 2022. Improving Generalization by Commonality Learning in Face Forgery Detection. *IEEE Transactions on Information Forensics and Security* 17 (2022), 547–558.

[69] Yuanhao Zhai, Tianyu Luan, David Doermann, and Junsong Yuan. 2023. Towards Generic Image Manipulation Detection with Weakly-Supervised Self-Consistency Learning. In *Proceedings of the IEEE/CVF International Conference on Computer Vision (ICCV)*. 22390–22400.

[70] Daichi Zhang, Zihao Xiao, Shikun Li, Fanzhao Lin, Jianmin Li, and Shiming Ge. 2024. Learning natural consistency representation for face forgery video detection. In *Proceedings of The 18th European Conference on Computer Vision (ECCV)*. Springer, 407–424.

[71] Hanqing Zhao, Wenbo Zhou, Dongdong Chen, Tianyi Wei, Weiming Zhang, and Nenghai Yu. 2021. Multi-Attentional Deepfake Detection. In *Proceedings of the IEEE/CVF Conference on Computer Vision and Pattern Recognition (CVPR)*. 2185–2194.

[72] Tianchen Zhao, Xiang Xu, Mingze Xu, Hui Ding, Yuanjun Xiong, and Wei Xia. 2021. Learning Self-Consistency for Deepfake Detection. In *Proceedings of the IEEE/CVF International Conference on Computer Vision (ICCV)*. 15023–15033.

[73] Yinglin Zheng, Jianmin Bao, Dong Chen, Ming Zeng, and Fang Wen. 2021. Exploring Temporal Coherence for More General Video Face Forgery Detection. In *Proceedings of the IEEE/CVF International Conference on Computer Vision (ICCV)*. 15044–15054.

[74] Jiaran Zhou, Yuezun Li, Baoyuan Wu, Bin Li, Junyu Dong, et al. 2024. FreqBlender: Enhancing DeepFake Detection by Blending Frequency Knowledge. In *Advances in Neural Information Processing Systems (NeurIPS)*, Vol. 37. 44965–44988.

[75] Tianfei Zhou, Wenguan Wang, Zhiyuan Liang, and Jianbing Shen. 2021. Face Forensics in the Wild. In *Proceedings of the IEEE/CVF Conference on Computer Vision and Pattern Recognition (CVPR)*. 5778–5788.

[76] Lianghui Zhu, Bencheng Liao, Qian Zhang, Xinlong Wang, Wenyu Liu, and Xinggang Wang. 2024. Vision mamba: efficient visual representation learning with bidirectional state space model. In *Proceedings of the 41st International Conference on Machine Learning (ICML)*. Article 2584, 14 pages.

[77] Xizhou Zhu, Han Hu, Stephen Lin, and Jifeng Dai. 2019. Deformable ConvNets V2: More Deformable, Better Results. In *Proceedings of the IEEE/CVF Conference on Computer Vision and Pattern Recognition (CVPR)*.

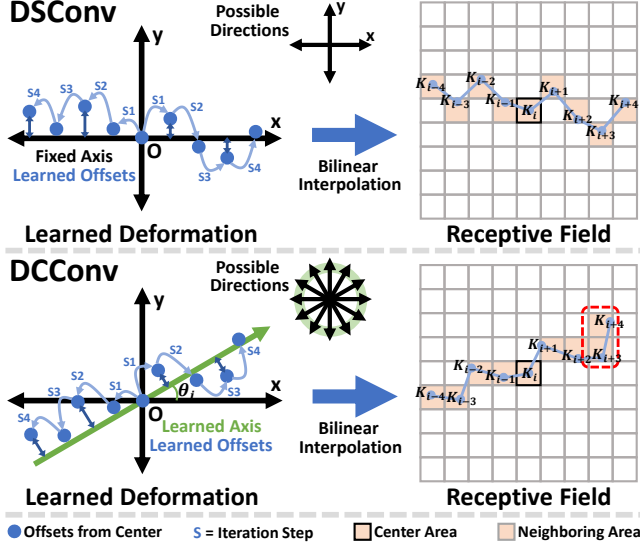


Figure 8: Visual comparison between DSConv and the proposed DCConv, initialized along the x-axis. DSConv learns perpendicular offsets to model slender structures oriented along a predefined direction. In contrast, DCConv predicts both perpendicular offsets and axis orientation, enabling it to represent slender geometries aligned in any direction. This added flexibility allows DCConv to capture a broader range of slender structures, including the shape highlighted in the red box, which DSConv is unable to model.

A Comparison Between DSConv & DCConv

Figure 8 visually compares DSConv with the proposed DCConv. DSConv captures slender structures by learning offsets aligned strictly along the x-axis or y-axis. In contrast, DCConv simultaneously predicts both the offsets and the axis orientation, allowing it to represent slender geometries in any direction. As a result, DCConv is capable of modeling a broader range of slender structures.

B Implementation Details

This study uses the synthetic data generation framework, preprocessing techniques, and data augmentation strategies in SBI [52].

B.1 Synthetic Data Generation.

The SBI framework generates fake face images from authentic face samples by mimicking the deepfake generation process. Specifically, a real image is first input into a Source-Target Generator (STG) and a Mask Generator (MG). The STG applies a series of image transformations (detailed later) to create pseudo source and target images, while the MG produces a blending mask based on pre-detected facial landmarks and further augments it to enhance diversity. Finally, the pseudo source and target images are blended using the generated mask, resulting in a pseudo-fake face sample.

B.2 Preprocessing.

The 81-point facial landmark shape predictor from Dlib [26] is utilized to extract facial landmarks, which are required exclusively

during the training phase. Additionally, the RetinaFace [7] is employed to generate facial bounding boxes. During training, the bounding box is cropped with a random margin ranging from 4% to 20%, while for inference, a fixed margin of 12.5% is applied.

B.3 Data Augmentation.

The image processing toolbox presented in [2] is employed for data augmentation. Within the STG of SBI, image transformations such as RGBShift, HueSaturationValue, RandomBrightnessContrast, Downscale, and Sharpen are applied to create pseudo source and target images. During the training phase, real samples undergo augmentations such as ImageCompression, RGBShift, HueSaturationValue, and RandomBrightnessContrast. These operations greatly improve the generalization capability of our model.

B.4 Other Details.

We sample eight frames from each video during training and 32 frames per video for inference. If a frame contains multiple detected faces, the classifier is applied to each face individually, and the highest fakeness score among them is selected as the predicted confidence for that frame. Additionally, the input images are resized to a spatial resolution of 224×224 during both training and testing.

Table 7: Cross-manipulation evaluation results for the HWFEB and DCConv. These two components effectively enhance the overall performance of our model.

Method	Test Set AUC (%)				
	DF	F2F	FS	NT	FF++
w/o HWFEB	100	99.93	99.87	98.38	99.55
w/o DCConv	99.99	99.97	99.87	98.83	99.67
The Proposed	100	99.98	99.94	98.88	99.70

Table 8: Ablation study results on different HWFEB stages.

Stages	Test Set AUC (%)								
	1	2	3	4	CDF	DFDC	DFDCP	FFIW	Avg.
✓					94.76	81.79	87.88	85.03	87.34
✓	✓				95.07	81.66	88.17	84.63	87.38
✓	✓	✓			95.99	82.79	89.44	86.95	88.79
✓	✓	✓	✓	✓	96.29	82.97	89.62	86.59	88.87

C Experimental Results

In this section, we present additional experimental results that are omitted from the main text due to space constraints.

C.1 Additional Analysis of HWFEB & DCConv.

The HWFEB integrates wavelet information into the VMamba model, while the DCConv effectively captures the slender structures of facial contours. As visually demonstrated in Figure 7, these components are instrumental in directing the model’s attention

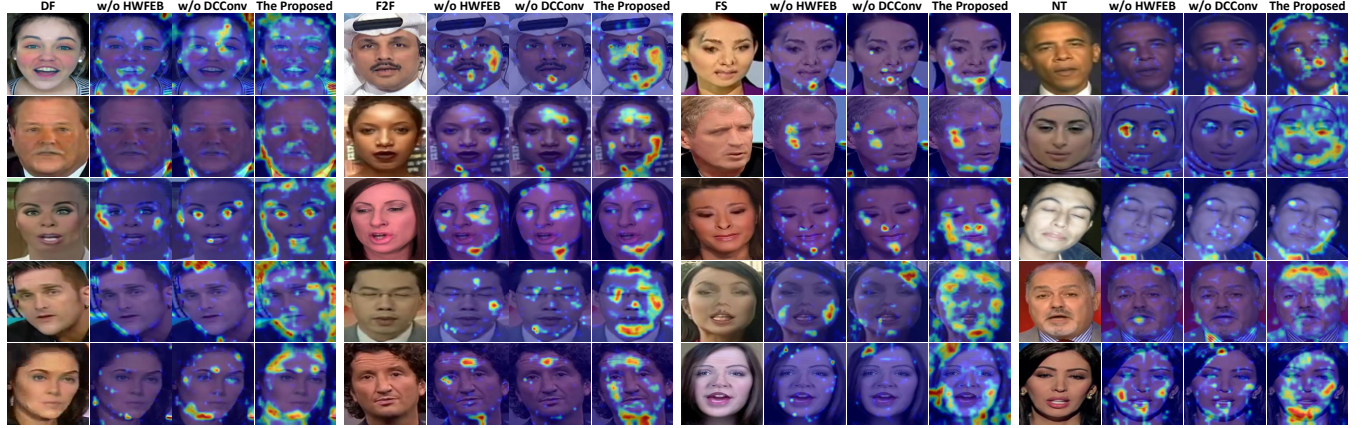


Figure 9: Saliency maps for a variety of fake samples from the FF++ dataset, where redder regions indicate areas of higher model attention. The HWFEB and DCCconv effectively direct our model’s attention toward critical facial contours.

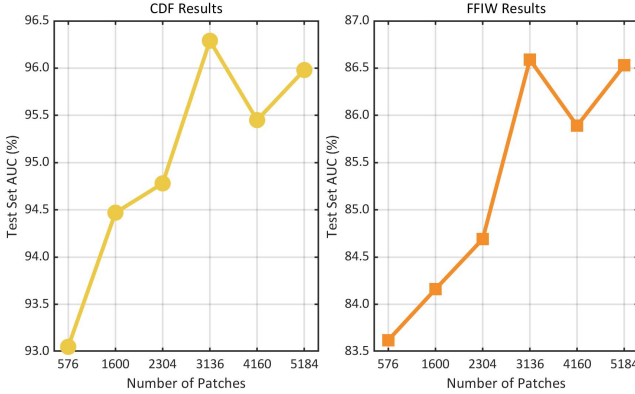


Figure 10: Effect of patch count on model performance. The horizontal axis shows the number of patches following the Stem module in the VMamba model. Overall, performance improves with an increase in patch count. Notably, the peak performance is observed at a patch count of 3136, which corresponds to an input size of 224×224 pixels, the same resolution utilized during the pretraining of VMamba-S.

Table 9: Ablation study results for scanning methods.

Method	Test Set AUC (%)			
	CDF	DFDC	DFDCP	FFIW
Single-directional Scan [13]	94.37	80.39	87.61	85.98
Bidirectional Scan [76]	95.40	81.32	88.42	86.47
Cross-Scan [35]	96.29	82.97	89.62	86.59

toward key facial contours, which are often rich in forgery artifacts. To further substantiate this observation, we present additional experimental results. As illustrated in Figure 9, incorporating HWFEB and DCCConv enhances the model’s ability to accurately focus on essential facial contours during decision-making. Moreover, the

cross-manipulation evaluation results in Table 7 highlight the contributions of these two components to the model’s performance. In Table 3, we assess the impact of applying DWT only at the first stage of the backbone. Here, we extend this analysis to examine the individual contributions of each HWFEB stage. The cross-dataset evaluation results in Table 8 indicate that all stages work together to enhance performance, validating our hierarchical design.

C.2 Additional Analysis of VMamba.

We investigate the effect of patch count on model performance by systematically varying the input image sizes. The cross-dataset evaluation results in Figure 10 reveal that, in general, model performance improves as the number of patches increases. The peak performance is observed at a patch count of 3136, which corresponds to an input size of 224×224 pixels, the same resolution used during the pretraining of the VMamba-S model. Based on these findings, we choose to maintain the pretraining resolution rather than arbitrarily increasing the input size. Additionally, we compare the cross-scan used in VMamba with single-directional [13] and bidirectional [76] scans. The cross-dataset evaluation results in Table 9 support the validity of our design choice.

C.3 Analysis of Kernel Length for DCCConv.

We systematically evaluate four different kernel lengths for DCConv. Based on the cross-dataset assessment results in Table 10, a kernel length of 9 is selected as it delivers the best performance.

C.4 Model Robustness.

To assess the robustness of our method, we conduct experiments across four real-world degradation conditions: compression, occlusion, noise, and blur. For compression, we apply the JPEG standard with quality settings of 95 (low), 85 (medium), and 75 (high). For occlusion, we randomly mask 2% (low), 5% (medium), and 10% (high) of the image pixels. For noise, we introduce Gaussian noise with standard deviations of 0.01 (low), 0.05 (medium), and 0.1 (high). For blur, we use Gaussian blur with kernel/sigma values of 5/1 (low), 7/2 (medium), and 9/3 (high). The cross-dataset results on the CDF

Table 10: Ablation study results on DCCConv’s length.

Length	Test Set AUC (%)				
	CDF	DFDC	DFDCP	FFIW	Avg.
5	95.13	82.67	87.10	86.10	87.75
7	95.66	82.99	88.94	86.97	88.64
9	96.29	82.97	89.62	86.59	88.87
11	95.70	81.89	89.18	86.06	88.21

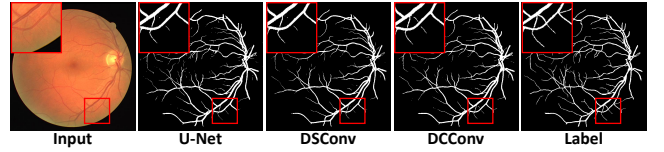
Table 11: Model robustness across various types and severities of image degradation. We compare WMamba with SBI [52].

Degradation	Method	ΔAUC by Severity (%)		
		Low	Medium	High
Compression	SBI [52]	-0.73	-1.66	-2.29
	WMamba	-0.52	-1.22	-2.13
Occlusion	SBI [52]	-24.71	-32.31	-36.08
	WMamba	-12.87	-22.71	-28.15
Noise	SBI [52]	-14.57	-29.75	-31.33
	WMamba	-7.20	-27.16	-29.01
Blur	SBI [52]	-3.20	-12.77	-20.30
	WMamba	-2.51	-9.51	-16.97

Table 12: Quantitative evaluation results on the DRIVE dataset. The proposed DCCConv achieves the best results.

Method	Evaluation Metric (%)		
	IoU	Dice	Avg.
U-Net [49]	66.57	79.90	73.24
U-Net + DSConv [47]	67.70	80.69	74.20
U-Net + DCCConv	68.70	81.41	75.06

dataset, shown in Table 11, demonstrate that WMamba consistently and significantly outperforms SBI across all degradation conditions, with particularly strong performance in occlusion scenarios.

**Figure 11: Qualitative evaluation results on the DRIVE dataset. Notably, DCCConv better segments subtle vessels.**

C.5 The Versatility of DCCConv.

We assess the versatility of DCCConv using the Digital Retinal Images for Vessel Extraction (DRIVE) dataset [55], a widely recognized benchmark for medical image segmentation. Notably, the segmentation targets in the DRIVE dataset exhibit slender structures, making it a suitable testbed for our approach. The dataset comprises 20 training and 20 testing images, each with dimensions of $565 \times 584 \times 3$. To facilitate training, we crop the original training samples into 4,000 smaller patches, each of size $64 \times 64 \times 3$. For our experiments, we integrate DCCConv into the U-Net architecture [49], replacing its standard convolutional layers. We then compare the performance of DCCConv-enhanced U-Net against two baselines: the original U-Net and a variant where the convolutional layers are replaced by DSConv [47]. To ensure a fair comparison, all methods are trained under the same experimental conditions. The training process leverages a combined objective function that integrates Dice Loss [41] and Focal Loss [33]. Each model is trained for 50 epochs with a batch size of 16 using the Adam optimizer. The initial learning rate is set to $1e-3$ and is reduced by half every 10 epochs. The quantitative evaluation results presented in Table 12, assessed using the Intersection over Union (IoU) and Dice metrics, demonstrate that our method achieves superior performance compared to others. Additionally, the qualitative evaluation results in Figure 11 highlight DCCConv’s exceptional capability to capture subtle and slender structures. Overall, these findings underscore the effectiveness of DCCConv as a versatile, plug-and-play module for improving the representation of slender structures.